

Internal Dynamics of the Hypercompact H II Region G28.20–0.04N

M. Sewilo¹, E. Churchwell², S. Kurtz³, W. M. Goss⁴, and P. Hofner^{4,5}

ABSTRACT

High resolution ($0''.15$) Very Large Array observations of 7 mm continuum and H53 α line emission toward the hypercompact H II region G28.20-0.04N reveal the presence of large-scale ordered motions. We find a velocity gradient of $10^3 \text{ km s}^{-1} \text{ pc}^{-1}$ along the minor axis of the continuum source. Lower resolution ($1''.0$ – $2''.3$) radio recombination line observations indicate a systematic increase of line width from H30 α to H92 α . Under the assumption that the H30 α line does not suffer significant pressure broadening, we have deconvolved the contributions of statistical broadening (thermal, turbulent, and pressure) from large-scale motions. The pressure broadening of the H53 α , H76 α , and H92 α lines implies an electron density of $6.9 \times 10^6 \text{ cm}^{-3}$, $8.5 \times 10^5 \text{ cm}^{-3}$, and $2.8 \times 10^5 \text{ cm}^{-3}$, respectively.

Subject headings: H II regions — radio lines: ISM — stars: formation

1. Introduction

Hypercompact (HC) H II regions have about one tenth the size ($<0.05 \text{ pc}$) and about a hundred times the density ($n_e > 10^5 \text{ cm}^{-3}$) of ultracompact (UC) H II regions. It has been postulated that HC H IIs represent the transition from hot molecular cores to UC H II regions (Kurtz 2000); that is, the transition from rapid accretion onto a massive central protostar to the termination of accretion and the emergence of a detectable radio H II region.

¹Space Telescope Science Institute, 3700 San Martin Drive, Baltimore, MD 21218, mmsewilo@stsci.edu

²University of Wisconsin - Madison, Department of Astronomy, 475 N. Charter St., Madison, WI 53706, churchwell@astro.wisc.edu

³Centro de Radioastronomía y Astrofísica, Universidad Nacional Autónoma de México, Apdo. Postal 3-72, 58089, Morelia, Mich. México, s.kurtz@astrosmo.unam.mx

⁴National Radio Astronomy Observatory, P.O. Box 0, Socorro, NM 87801, mgoss@aoc.nrao.edu

⁵New Mexico Tech, Physics Department, 801 Leroy Place, Socorro, NM 87801, phofner@nrao.edu

If HC H IIs occupy this evolutionary niche, they should show evidence of ordered large-scale motions such as expansion, infall, bipolar outflows, rotation and shocks due to accretion and outflows. Also, owing to their high electron densities, recombination lines from the H^+ gas should suffer substantial pressure broadening in high quantum state radio recombination lines (RRLs).

It is not clear if HC H II regions are simply smaller and denser versions of UC H II regions or if they are intrinsically different. Their relative sizes, however, suggest that stellar clusters may be responsible for UC H II regions, while HC H II regions may be produced by a single, or perhaps a binary, OB protostar. Some, but not all, HC H IIs have unusually broad radio recombination lines (BRRLs) with full widths at half maximum intensity (FWHM) $>40 \text{ km s}^{-1}$. The typical FWHM of more evolved (UC and compact) H II regions is $\sim 25\text{-}30 \text{ km s}^{-1}$ in all RRLs from principal quantum states $n < 100$. The fact that not all HC H IIs have BRRLs may imply that BRRLs are only present for a limited period during the earliest HC H II evolutionary phase when ordered large-scale motions are maximum.

Sewilo et al. (2004, and in prep.) observed the $H92\alpha$, $H76\alpha$, and $H53\alpha$ lines toward the HC H II region G28.20-0.04N (hereafter G28.20N) with resolutions of $2''.3$, $1''.5$, and $1''.6$, respectively, all of which are larger than the angular size of the HC H II region. They found FWHMs of 74 km s^{-1} , 58 km s^{-1} , and 40 km s^{-1} , respectively. The rapid change in line width with transition strongly suggests that pressure broadening is a dominant broadening mechanism in G28.20N.

We have chosen G28.20N for a high resolution $H53\alpha$ study to determine the origin of the BRRLs in this source because: it is a bona fide HC H II region; it has already been observed in several RRLs at lower angular resolution; several masers have been detected toward G28.20N implying extreme youth (H_2O - Han et al. 1998; OH 6035 MHz - Caswell & Vaile 1995; OH 1667 MHz - Argon et al. 2000; and, CH_3OH - Menten 1991). The $H53\alpha$ line was chosen because it should be mostly free from pressure broadening, the nebula should be optically thin at this frequency, and the Very Large Array can achieve an angular resolution one tenth that of previous observations at 43 GHz.

2. Observations

G28.20N was observed with the VLA¹ at 7 mm (continuum and H53 α line) with an angular resolution of 0".15. The observations were made on 2004 January 19 with the VLA in its B-configuration. At the H53 α rest frequency of 42.95197 GHz, this provided an angular resolution of 0".17 \times 0".13 at a position angle of $-4^\circ.8$. A 25 MHz bandwidth was employed, with 31 spectral line channels of 781 kHz each. This provided a velocity resolution of 5.5 km s⁻¹, which was later Hanning smoothed to 11 km s⁻¹. Integration time on-source was about 1.4 hours. 3C 286 (1.47 Jy), 1851+005 (0.68 \pm 0.01 Jy), and 3C 345 (4.81 \pm 0.18 Jy) were used as flux density, phase and bandpass calibrators, respectively. The data reduction, including self-calibration, followed the VLA high-frequency guidelines for calibration and imaging, using the NRAO package AIPS. The continuum image is shown in Figure 1. Continuum-subtracted line images were used to generate H53 α maps.

3. Results

3.1. Morphology of the Source

At our high angular resolution, G28.20N appears as a shell-like structure, extended in the SE-NW direction (Figure 1). There are two peaks, separated by 0".36 (2050 AU or 0.01 pc at a distance of 5.7 kpc; Fish et al. 2003). The brightness distributions along one-dimensional cuts through the source show a well-defined shell with low intensity at the center. The center of the shell-like nebula is at RA = 18^h42^m58^s.11 and Dec = $-04^\circ 13' 57''.4$ (J2000). The source diameter at 10% of the peak (the 12 σ contour in Figure 1) is $\theta_s = 0''.9$ (5100 AU; where $\theta_s = (\theta_{RA} \cdot \theta_{Dec})^{1/2}$). The integrated flux density is 645 \pm 65 mJy, where the 10% uncertainty reflects VLA calibration uncertainty in the 7 mm band. The synthesized beam brightness temperature using the peak brightness of 64 mJy beam⁻¹ (located at the W side of the shell) is 1920 K, implying a peak optical depth of 0.3 based on $T_e = 7000$ K, and a peak emission measure (EM) of 1.6×10^9 pc cm⁻⁶. This EM implies an rms electron density of $n_e = 6.2 \times 10^5$ cm⁻³. The synthesized beam brightness of the central cavity, 11 mJy beam⁻¹, corresponds to 343 K, implying an optical depth of 0.05, an EM of 2.5×10^8 pc cm⁻⁶, and an rms n_e of 2.5×10^5 cm⁻³.

¹The Very Large Array (VLA) is operated by the National Radio Astronomy Observatory (NRAO), a facility of the National Science Foundation operated under cooperative agreement by Associated Universities, Inc.

3.2. Velocity Structure

We examined the velocity structure of G28.20N by making contour plots of the H53 α emission, using moment maps, position-velocity diagrams, and by Gaussian fitting of the line profiles at multiple positions. All these methods reveal a velocity gradient of $10^3 \text{ km s}^{-1} \text{ pc}^{-1}$, with velocities increasing from the NE to SW.

In Figure 2 we show least-squares Gaussian fits to the H53 α line integrated over different areas of the source, each approximately one synthesized beam in size. The positions are indicated in the continuum image of Figure 2. The boxes are located along the major and minor axes of the shell, with two boxes (B and D) sampling the regions of maximum emission. Box C covers the low intensity central region, while boxes F and I trace an extension in the SE–NW direction. We also analyzed the line emission integrated over the entire source (Box J). The parameters of the Gaussian fits are given in Table 1; V_{LSR} is the velocity relative to the local standard of rest, FWHM_{deconv} is the line FWHM corrected for instrumental broadening, S_L is the flux density in excess of the continuum at line center, and S_C is the continuum flux density. In some directions (e.g. E and H) the line profiles are asymmetric with an additional velocity component apparent. All the asymmetries occur in the velocity range of $\sim 110\text{--}130 \text{ km s}^{-1}$. Although weak, these features are real; we also detect a 130 km s^{-1} component in the H76 α line.

The sequence of five H53 α line profiles shown in Figure 2 indicates a systematic shift in the central line velocity from the NE to SW. The dotted vertical line indicates the 88.2 km s^{-1} systemic velocity of the nebula obtained from H53 α data taken with 10 times lower resolution than shown in boxes A–E (*upper right*; HPBW $\sim 1.''6$)². Thus, the centroid velocity of $\sim 78 \text{ km s}^{-1}$ in Box A (NE side of G28.20N) is *blueshifted* and the centroid velocity of $\sim 97 \text{ km s}^{-1}$ in Box E (SW side of G28.20N) is *redshifted* with respect to the systemic nebular velocity. The H53 α lines suggest rotational motion with the axis of rotation in the SE–NW direction. There is no velocity pattern along the elongated SE–NW axis (i.e. no indication of an outflow along this axis). We suggest that the excess line broadening along this axis may be due to an outflow in the plane of the sky, expanding perpendicular to its axis of flow with a velocity of $\sim 5 \text{ km s}^{-1}$.

²Our 7 mm flux density and H53 α line width (both B- and D-array) disagree with the results of Keto et al. (2008) for their 7 mm/H53 α data ($S_{\text{int}}=1.1 \text{ Jy}$ and $\text{FWHM} = 33.4 \pm 1.5 \text{ km s}^{-1}$). To investigate this discrepancy, we re-reduced our lower resolution 7 mm data and the archival Keto et al. data (AK607) using consistent procedures for both data sets. We confirmed our results and found that the Keto et al. data are consistent with our own. For the AK607 data we find an integrated 7 mm continuum flux density of $790 \pm 35 \text{ mJy}$ and a FWHM for the H53 α line of $38.7 \pm 0.9 \text{ km s}^{-1}$.

The velocity structure observed in G28.20N is consistent with a torus rotating with a velocity of 5.0 km s^{-1} at a radius of 0.005 pc (1030 AU ; at the position of the peaks), which corresponds to a velocity gradient of about $10^3 \text{ km s}^{-1} \text{ pc}^{-1}$ or an interior mass of $28 M_{\odot}$ for Keplerian motion.

3.3. Optical Depth Effects

We compared integrated line profiles for all transitions and found that the $\text{H}30\alpha$ line velocity shifts by about $5\text{-}14 \text{ km s}^{-1}$ with respect to the $\text{H}92\alpha$, $\text{H}76\alpha$, and $\text{H}53\alpha$ lines. The $\text{H}92\alpha$, $\text{H}76\alpha$, and $\text{H}53\alpha$ line velocity integrated over the nebula is $82.9\pm 0.9 \text{ km s}^{-1}$, $78.9\pm 0.8 \text{ km s}^{-1}$, and $88.2\pm 0.4 \text{ km s}^{-1}$, respectively. Keto et al. (2008) reports the $\text{H}30\alpha$ line velocity of $92.5\pm 0.2 \text{ km s}^{-1}$. A similar trend of increasing RRL velocity with increasing frequency has been reported for other compact H II regions, e.g., W49A/B (De Pree et al. 1997) and W3(OH) (Berulis & Ershov 1983). Welch & Marr (1987) and Keto et al. (1995) proposed that this is an optical depth effect, in which deeper layers with different velocities are probed at higher frequencies. Following their arguments, the optical depth decreases rapidly at high frequencies because the absorption coefficient is inversely proportional to the square of the frequency; thus the $\text{H}92\alpha$, $\text{H}76\alpha$, $\text{H}53\alpha$, and $\text{H}30\alpha$ emission arise from different volumes of gas with $\text{H}30\alpha$ emission being more sensitive to the denser regions. They also argue that the velocity of the high frequency RRLs provides a good approximation to the average motion of the H II region provided that the random motions are the same for all densities throughout the nebula. The velocity of this innermost H II gas is expected to most closely indicate the stellar velocity; hence, for G28.20N, the $\text{H}30\alpha$ line velocity should provide the best estimate of the central star’s radial velocity. The blueshifted velocities of the outer H II region, traced by the $\text{H}92\alpha$, $\text{H}76\alpha$, and $\text{H}53\alpha$ lines, imply expansion, consistent with a strongly over-pressured nebula.

4. Line Broadening Mechanisms: Pressure Broadening vs. Dynamic Motions

Keto et al. (2008) detected the $\text{H}30\alpha$ line toward G28.20N using the SMA with an angular resolution of $1''$. The width of the $\text{H}30\alpha$ line is $20.9\pm 0.6 \text{ km s}^{-1}$. At the high frequency of the $\text{H}30\alpha$ line, line width should be dominated by the thermal, turbulent, and large scale motions; pressure broadening is negligible due to the rapid decrease in pressure broadening with frequency. Thermal and turbulent broadening produce convolved Gaussian profiles whose center velocities generally coincide. Large-scale coherent motions can produce velocity-shifted profiles that may deviate from Gaussian shapes. The observed profiles de-

pend on the type and angular extent of the large-scale velocity components relative to the synthesized beam. In particular, as the angular resolution is increased, each resolution element should approach the combined thermal plus turbulent broadening of the gas, with its central velocity reflecting the dominant large-scale motion of the gas in that volume element. In some cases, two components of large-scale coherent motions may fall within a single beam, which may result in a double Gaussian. An example of this is an expanding bubble whose front and back faces are included in all observations or if the red and blue lobes of an outflow are projected onto the same resolution element.

Molecular line observations of UC H II regions and massive cloud cores suggest that the typical molecular line width where HC H II regions form is ~ 5 km s⁻¹ (FWHM; Cesaroni et al. 1991, Plume et al. 1997). We adopt this value for the non-thermal (turbulent) contribution to the line width since the thermal width for molecules is < 0.5 km s⁻¹. For 7000 K, the thermal contribution to the line width is 17.9 km s⁻¹ (FWHM). Thus, the combined contribution (added in quadrature) of thermal and turbulent widths to a RRL profile is 18.6 km s⁻¹. We can determine the contribution from kinematic motions by subtracting this value in quadrature from the observed H30 α line width. The residual after accounting for thermal and turbulent motion is 9.6 km s⁻¹. This excess represents the approximate magnitude of the large-scale motions (detected in the H53 α line) within G28.20N as the data is averaged over the entire source. For non-thermal widths of 0 km s⁻¹ (no turbulent motions) and 10 km s⁻¹, the contribution from large-scale motions would be 10.8 km s⁻¹ and 4.1 km s⁻¹, respectively. The value of the non-thermal contribution to the line width is not essential to the following calculations of pressure broadening.

The line width in km s⁻¹ arising from thermal and turbulent motions is constant for all relevant transitions (from H30 α to H92 α). Thus, we can determine the influence of internal kinematics on the H53 α , H76 α , and H92 α line widths. The subtraction in quadrature of the 9.6 km s⁻¹ kinematic broadening from the observed line widths (39.7 ± 1.3 , 57.6 ± 2.2 , and 74.4 ± 2.6 km s⁻¹) gives FWHMs of 38.5, 56.8, and 73.8 km s⁻¹ for the H53 α , H76 α , and H92 α lines, respectively; these line widths, “corrected” for kinematic broadening, still contain a pressure broadening contribution.

To estimate the pressure broadening of the H53 α , H76 α , and H92 α lines, we use an approximation for the Voigt profile width (Gordon & Sorochenko 2003, eq. 2.72), which relates the frequency widths of the Gaussian, Lorentz and Voigt profiles. The Gaussian width for low frequency lines is determined from the width of a high frequency line, unaffected by pressure broadening. Here we use the 16.167 MHz H30 α line width. For the H53 α line, the Gaussian width is 2.99 MHz and the observed line width is 5.69 MHz, implying a pressure broadening width of 4.03 MHz (or 28.1 km s⁻¹). For the H76 α line, the Gaussian width is

1.02 MHz and the observed line width is 2.82 MHz, implying a pressure broadening width of 2.43 MHz (or 49.5 km s^{-1}). For the H92 α line, the Gaussian width is 0.58 MHz and the observed line width is 2.06 MHz, implying a pressure broadening width of 1.89 MHz (or 68.1 km s^{-1}).

The pressure broadening width is proportional to $n^{7.4} T_e^{-0.1} n_e$; thus, the pressure broadened lines can be used to determine the true space electron density n_e averaged over the nebula (Brocklehurst & Seaton 1972). Using T_e of 7000 K, we find n_e of $(6.9 \pm 0.4) \times 10^6 \text{ cm}^{-3}$, $(8.5 \pm 0.4) \times 10^5 \text{ cm}^{-3}$ and $(2.8 \pm 0.1) \times 10^5 \text{ cm}^{-3}$ based on the H53 α , H76 α , and H92 α lines, respectively. The rms electron densities inferred from the 0.7, 2, and 3.6 cm continuum observations are $1.7 \times 10^5 \text{ cm}^{-3}$, $9.3 \times 10^4 \text{ cm}^{-3}$ (Sewilo et al. 2004, and in prep.), and $7.6 \times 10^4 \text{ cm}^{-3}$ (Sewilo et al. 2004), respectively. The higher electron density from pressure broadening is expected because it represents the actual space density of the gas that produces the broad lines as opposed to the rms density derived from the radio continuum. The fact that the average density decreases with higher quantum transitions also suggests that each line in the range 0.7 to 3.6 cm samples different volumes of gas, as also suggested by the change in line velocity with transition.

The rms and true electron densities can be used to calculate the filling factor f for the nebula. Equating the Strömngren relation for a uniform density region (in terms of n_{rms}) with that of a clumpy region (in terms of n_{true}) which is formed of N smaller clumps, one obtains $N r_{clump}^3 / r_{uniform}^3 = n_{e,rms}^2 / n_{e,true}^2 = f$. This is the ratio of the volume occupied by the dense gas to the total volume of the H II region; thus f is a measure of the degree of clumpiness of the nebula. Based on the 7 mm continuum and line data, we calculated the filling factor of 6×10^{-4} for the highest density gas we sample in G28.20N.

5. Summary

We have resolved the morphology and velocity structure of the HC H II region G28.20N. The continuum emission has a shell-like structure, with an inner radius of 1100 AU, an outer radius of 2500 AU, and an rms density contrast of 2-3 between the central cavity and the torus.

Under the assumption that the H30 α line is not significantly pressure broadened and that turbulence broadening is $\sim 5 \text{ km s}^{-1}$, we have resolved the contributions of thermal, turbulent, and pressure broadening from large-scale ordered motions. We suggest that the ordered motion has two components: a velocity gradient of $10^3 \text{ km s}^{-1} \text{ pc}^{-1}$ in the NE–SW direction along the minor axis which may indicate rotation of a torus around a $28 M_\odot$

object; and line broadening (line splitting at some points) along the major axis which may indicate lateral expansion of an outflow along the major axis of the nebula. In this scenario, the outflow axis would have to be in the plane of the sky because line velocities along this axis are centered on the systemic velocity of the nebula. We suggest that the excess line broadening along the major axis is due to expansion of the outflow perpendicular to its axis.

The line width from large scale motions averaged over the whole nebula is $\sim 10 \text{ km s}^{-1}$. We find pressure broadening line widths for the $\text{H}53\alpha$, $\text{H}76\alpha$, and $\text{H}92\alpha$ lines of ~ 28 , ~ 50 , and $\sim 68 \text{ km s}^{-1}$, respectively. These spatially unresolved, pressure broadened lines were used to determine electron densities averaged over the nebula (not rms densities). The mean n_e is $6.9 \times 10^6 \text{ cm}^{-3}$, $8.5 \times 10^5 \text{ cm}^{-3}$, and $2.8 \times 10^5 \text{ cm}^{-3}$ based on the $\text{H}53\alpha$, $\text{H}76\alpha$, and $\text{H}92\alpha$ lines, respectively. These densities are 4–40 times higher than the rms densities derived from continuum data. The fact that the average electron densities decrease with higher quantum transitions is consistent with the change in opacity with frequency.

This study has for the first time resolved the contributions of thermal, turbulent, pressure, and ordered large-scale motions of BRRLs in a hypercompact H II region. The observations show that large scale dynamics and high densities both contribute to BRRLs in G28.20N. This study was possible only because of the high angular resolution and sensitivity provided by the VLA.

We thank Michael Burton, the referee, for useful suggestions that improved our manuscript. M. S. and E. B. C. acknowledge partial support from NSF grant AST-0303689. S. K. acknowledges partial support from DGAPA, UNAM grant IN106107.

REFERENCES

- Argon, A. L., Reid, M. J., & Menten, K. M. 2000, *ApJS*, 129, 159
- Berulis, I. I., & Ershov, A. A. 1983, *Soviet Astr. Lett.*, 9, 341
- Brocklehurst, M., & Seaton, M. J. 1972, *MNRAS*, 157, 179
- Caswell, J. L., & Vaile, R. A. 1995, *MNRAS*, 273, 328
- Cesaroni, R., Walmsley, C. M., Kompe, C., & Churchwell, E. B. 1991, *A&A*, 252, 278
- De Pree, C. G., Mehringer, D. M., & Goss, W. M. 1997, *ApJ*, 482, 307
- Fish, V. L., Reid, M. J., Wilner, D. J., & Churchwell, E. 2003, *ApJ*, 587, 701

- Gordon, M. A., & Sorochenko, R. L. 2003, *Radio Recombination Lines: Their Physics and Astronomical Applications*, Series: Astrophysics and Space Science Library, Vol. 282
- Han, F., Mao, R. Q., Lu, J., Wu, Y. F., Sun, J., Wang, J. S., Pei, C. C., Fan, Y., Tang, G. S., & Ji, H. R. 1998, *A&AS*, 127, 181
- Keto, E., Welch, W. J., Reid, M. J., & Ho, P. T. P. 1995, *ApJ*, 444, 765
- Keto, E., Zhang, Q., & Kurtz, S. 2008, *ApJ*, 672, 423
- Kurtz, S. E. 2000, *RMxAC*, 9, 169
- Menten, K. M. 1991, *ApJ*, 380, L75
- Plume, R., Jaffe, D. T., Evans, N. J., II, Martin-Pintado, J., & Gomez-Gonzalez, J. 1997, *ApJ*, 476, 730
- Sewilo, M., Churchwell, E., Kurtz, S., Goss, W. M., & Hofner, P. 2004, *ApJ*, 605, 285
- Welch, W. J., & Marr, J. 1987, *ApJ*, 317, L21

Table 1. Gaussian Fits to the High Resolution H53 α RRLs^a

Box	V_{LSR} (km s ⁻¹)	$\text{FWHM}_{\text{deconv}}$ (km s ⁻¹)	S_L (mJy)	S_C (mJy)
A	77.6 ± 1.7	34.9 ± 4.9	5.1 ± 1.0	12.1 ± 0.6
B	85.8 ± 0.5	33.8 ± 1.3	22.5 ± 1.1	53.4 ± 0.6
C	92.1 ± 0.7	35.9 ± 2.2	6.7 ± 0.6	23.2 ± 0.6
D	95.8 ± 0.4	31.6 ± 1.0	26.4 ± 1.1	66.5 ± 0.6
E ^b	97.3 ± 1.0 127.9 ± 3.0	28.9 ± 3.0	7.8 ± 1.0	17.9 ± 0.6
...		9.4 ± 5.0	1.8 ± 1.3	...
F	89.9 ± 1.3	29.6 ± 3.7	4.0 ± 0.7	10.4 ± 0.6
G	87.7 ± 0.8	36.6 ± 2.4	11.4 ± 1.0	29.5 ± 0.6
H ^b	82.8 ± 1.7 110.3 ± 4.0	26.5 ± 3.3	10.1 ± 1.7	34.7 ± 0.6
...		21.1 ± 7.4	3.6 ± 1.8	...
I	83.2 ± 2.1	28.1 ± 5.9	3.4 ± 0.9	8.5 ± 0.6
J	89.5 ± 0.6	39.8 ± 1.7	238 ± 14	641 ± 4

^aSpectra were Hanning smoothed to a resolution of 11.0 km s⁻¹. Uncertainties are the formal 1 σ (68.3% confidence level) deviations of the data from the Gaussian fits.

^bTwo Gaussian components were required to adequately fit the observed line profile.

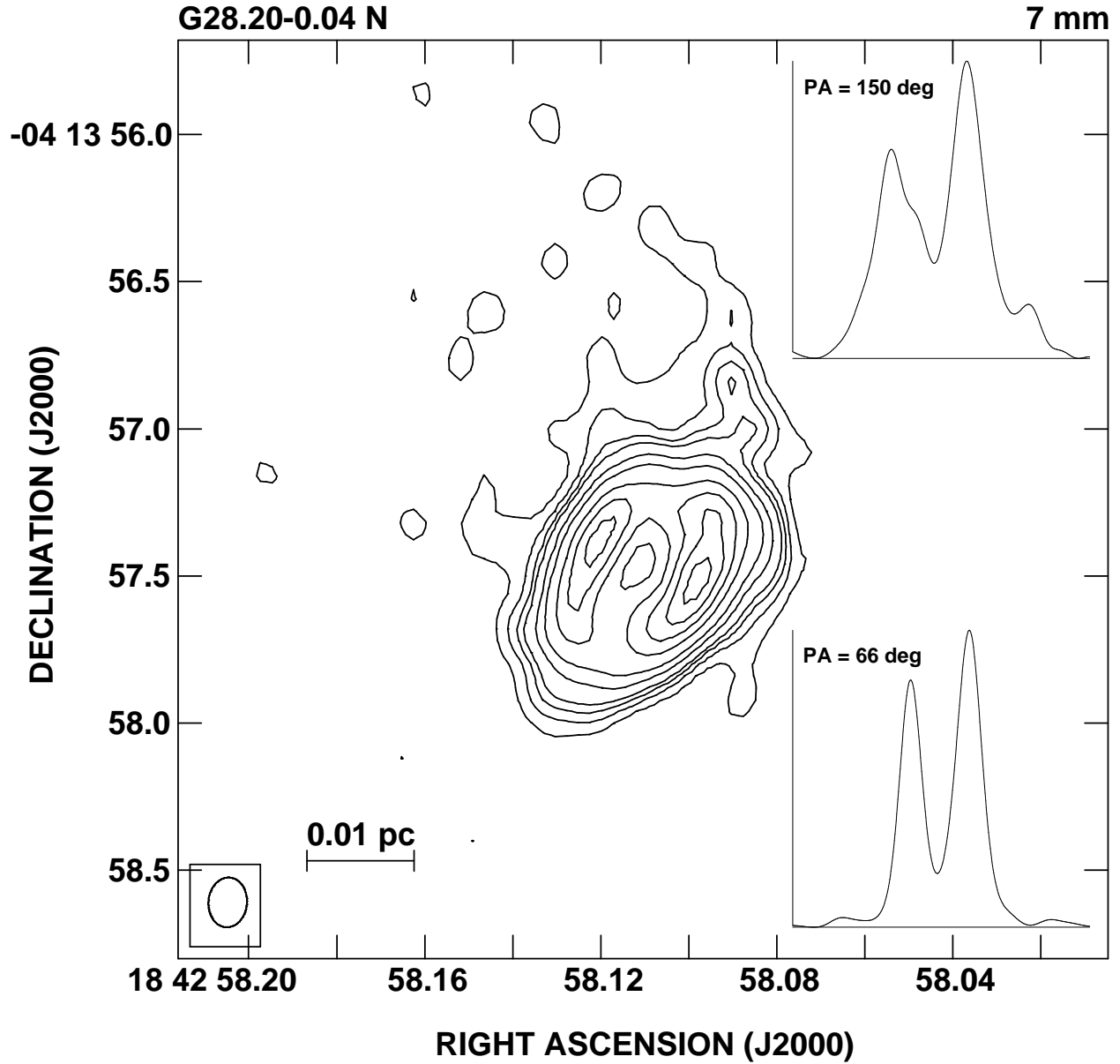


Fig. 1.— The 7 mm image of G28.20–0.04 N. The continuum intensity peak is $64.0 \text{ mJy beam}^{-1}$. The contours are $-3, 3, 6, 9, 12, 20, 30, 50, 70, 90, 110 \times 0.53 \text{ mJy beam}^{-1}$ (the image rms). The synthesized beam of $0''.17 \times 0''.13$ is shown in the lower left corner. The insets show intensity cuts through G28.20N; position angles indicate rotation East from North.

